NORTHWESTERN UNIVERSITY

Flexoelectricity in Polycrystalline $SrTiO_3$ Ceramics

Binghao (Evan) Guo

Advisers
Prof. Laurence D. Marks
Christopher A. Mizzi

Submitted in partial fulfillment of the requirements for the degree of

Bachelor of Science with Honors

Department of Materials Science and Engineering
Northwestern University
Evanston, IL

June 2019

Acknowledgments

This thesis would not have been possible without the guidance and support of many people. My thesis adviser, Prof. Laurence Marks, gave me the opportunity to conduct research as an undergraduate, and taught me lessons on scientific thinking that I will always cherish. My mentor, Christopher Mizzi, spent untold hours working closely with me, and inspired me with his enthusiasm and dedication to research. I credit to Laurie and Chris a large part of my decision to pursue a PhD. *Our* thesis course instructor, Prof. Kathleen Stair, helped not only me, but also the entire MSE senior class navigate the formidable process of completing a thesis, and encouraged us in stressful moments of the academic quarter.

My gratitude extends to other members of the L. D. Marks group that I came to know personally: Dr. Tassie Andersen, Dr. Seyoung Cook, Dr. Lawrence Crosby, Emily Greenstein, Dr. Pratik Koirala, Alex Lin, Tiffany Ly, Zachary Mansley, Ryan Paull, Dr. Betty Peng, Elizabeth Steele, and Dr. Xiao-xiang Yu. Thank you for welcoming me into the group family, for abundantly assisting me, and for showing me how good science is done.

Parts of this thesis also relied on generous assistance from members of the greater MSE community at Northwestern: Maxwell Dylla, Dr. Matthew Lu, Dr. Christos Malliakas, Dr. Carla Shute, Dr. Michael Yeung, and Weizi Yuan. Thank you for the new friendships and for sharing with me your knowledge and expertise.

Lastly, I want to acknowledge my parents, my brother, and my friends. Thank you for unconditionally supporting me and for giving me perspective on this journey through college.

The work presented in this thesis was funded by the US Department of Energy on grant # DE-FG02-01ER45945, titled *Oxide Surfaces: Unexpected Flexoelectricity and New Phenomena.*

Abstract

A material's ability to electrically polarize under a mechanical deformation is a highly desirable property with extensive applications in sensing and actuation. Current technologies rely heavily on piezoelectricity, which places a symmetry limitation on materials selection, and often involves the use of lead-based components. Flexoelectricity, the coupling of polarization to strain gradient, offers a solution to these issues since it exists independent of material symmetry. Beginning in 2001, experimental measurements of unexpectedly large flexoelectricity in high-κ ceramics drew significant attention to the flexoelectric field. Most of the later work has focused on the flexoelectric effect in single crystal oxides; their structural and chemical homogeneity make them ideal systems for studying the basic physics of flexoelectricity. However, expanding functionality enabled by flexoelectricity will almost certainly involve ceramics, which requires understanding the role played by microstructure.

In this work, the impact of ceramic microstructure on flexoelectricity was explored using the model cubic perovskite strontium titanate $SrTiO_3$. Polycrystalline $SrTiO_3$ samples were prepared by a solid-state sintering process. The average grain size was varied from 2-12 μm by controlling the sintering time. Structural characterization by X-Ray diffraction and dielectric measurements with impedance spectroscopy showed the samples to be cubic $SrTiO_3$ as expected. Polycrystalline samples with short sintering times displayed flexoelectric responses an order of magnitude greater than that of single crystal $SrTiO_3$, while samples with longer sintering times approached the single crystal values. Incidentally, the flexoelectric response was found to decrease over time. It is speculated that this decrease comes from a combination of factors related to sample degradation.

Table of Contents

List of Figures

List of Abbreviations

DMA Dynamic Mechanical Analyzer

FcV Flexocoupling Voltage

FxE Flexoelectric

GB Grain Boundary

LIA Lock-In Amplifier

SEM Scanning Electron Microscopy

STEM Scanning Transmission Electron Microscopy

STO Strontium Titanate ($SrTiO_3$)

TPB Three Point Bending

XRD X-Ray Diffraction

Chapter 1

Introduction

Materials capable of converting mechanical energy into electrical energy (and *vice versa*) enable a wide range of modern technologies. These electromechanical materials can be found in sonar sensors used for navigation and defense purposes, ultrasound devices used for medical imaging and quality control, and everyday low-cost alarms and microphones. Currently, these applications utilize the piezoelectric effect, which describes the coupling between electric polarization and mechanical strain. This effect, however, can only exist in materials that are noncentrosymmetric, thus placing a strong symmetry restriction on materials selection. Furthermore, common piezoelectric materials used in industry contain lead as a component, which can introduce toxic hazards during the materials processing stage.[1]

Flexoelectricity, the coupling of electric polarization to mechanical strain gradient, offers an alternative to piezoelectricity, and presents a solution to these issues since it exists in all dielectric materials independent of material symmetry. But in spite of the ubiquity of flexoelectricity, studies of this effect remained scarce long after it was theoretically proposed in 1964.[2] Early estimates had deemed the flexoelectric (FxE) effect negligible compared to the well-studied piezoelectric effect.[3] However, in the 2000s, experimental measurements of unexpectedly large flexoelectricity in high-κ ceramics drew significant attention to this field, and directed research efforts towards the study of oxide materials systems.[4–9] Incidentally, the FxE effect has gained increased recognition in nanoscience since large strain gradients are common at the nanoscale and can lead to large polarizations in materials with modest FxE properties.[3]

1.1 Fundamentals of Flexoelectricity

Flexoelectricity can be present as either strain gradient-induced polarization (the direct FxE effect) or polarization gradient-induced strain (the converse FxE effect).[3] In the case of the direct FxE effect, the constitutive equation is:

$$P_i = \mu_{ijkl} \frac{\partial \epsilon_{kl}}{\partial x_j} \tag{1.1.1}$$

where P_i is a component of the polarization, ϵ_{kl} is a component of the strain, x_j is the direction of the strain gradient, and the proportionality factor μ_{ijkl} is the FxE coefficient. It is worth noting here that both the direct and converse effects share the same FxE coefficients. Since P_i is a first-rank tensor property and $\partial \epsilon_{kl}/\partial x_j$ is a third-rank tensor property, μ_{ijkl} is a fourth-rank tensor property, which is necessarily non-zero for all dielectric solids (another common fourth-rank tensor property is elasticity).[10] As mentioned earlier, the ubiquitous nature of the FxE effect distinguishes it from the piezoelectric effect, which is a third rank tensor property that is only sustained in noncentrosymmetric materials. The underlying physical argument here is that in order to induce polarization, centrosymmetry needs to be broken. This can either be achieved internally/inherently by the material itself (piezoelectricity) or externally by the stimulus (flexoelectricity).

To facilitate comparison of the FxE effect across materials with different dielectric constants, it is convenient to introduce another parameter to quantify a FxE response: the flexocoupling voltage (FcV). In the simplified one-dimensional case, the FcV can be defined as:

$$f = \frac{\mu}{\varepsilon_0 \varepsilon_r} \tag{1.1.2}$$

where f is the FcV, μ is the FxE coefficient, ε_0 is the permittivity of free space, and ε_r is the dielectric constant. Early theoretical predictions suggested that the FcV should be within the range of 1-10 V for all materials, but it is now known that the FcV routinely exceeds the upper limit of this predicted range.[3, 11]

1.2 Extrinsic Contributions in Polycrystalline Materials

Most experimental studies of flexoelectricity have focused on single crystal systems due to their ideality, i.e. structural and chemical homogeneity.[3] However, as opposed to single crystals, common functional materials are polycrystalline and contain a variety of imperfections that can play a key role in determining their useful properties.[12] The presence of these imperfections within the microstructure raises the question of whether findings from the recent surge of single crystal studies can be directly applied to materials better suited for practical applications.[3, 11] Ultimately, the need for expanding functionality enabled by flexoelectricity will almost certainly require an understanding of the role played by the microstructure.

To experimentally approach flexoelectricity in polycrystalline materials inevitably requires analyzing the total FxE response. In this context, it is useful to view the total FxE response as having three separate contributions: (1) lattice contributions, such as the bulk FxE response of pure single crystals; (2) extrinsic contributions, such as grain/domain boundaries and other microstructural features; and (3) FxE low activity or inactive contributions, such as elastic deformations with minimal polarization. Examples of low activity contributions include grain boundary sliding and dislocation motion. The latter two contributions are expected to play a critical role in the FxE response of polycrystalline materials, analogous to how such contributions can affect other elastic and electrical properties.[12] A specific example can be found in prior work on $LaAlO_3$, where it was demonstrated that samples with twin domain walls have FxE coefficients nearly a factor of 5 greater than twin-free samples.

The remaining parts of this section examine two possible extrinsic contributions to the FxE response in strontium titanate $SrTiO_3$ (STO), a well-studied cubic oxide perovskite. At room temperature and atmospheric pressure, STO adopts the $Pm\bar{3}m$ space group.[13] STO was chosen as the model material system in this thesis due to the fact that it is the only material for which the full FxE tensor has been measured.[14] Additionally, the centrosymmetric crystal structure of STO at room temperature precludes any concerns of bulk piezoelectric contributions to measurements of FxE polarization.

1.2.1 Polar Grain Boundaries

In the context of FxE studies, polar grain boundaries (GB) are perhaps the most obvious and most important microstructural features to consider in STO ceramics. “Polar” means that there is a

net polarization associated with the GB structure, while the bulk material is otherwise nonpolar. When performing FxE measurements of STO ceramics, it is suspected that polar GBs in certain orientations will contribute to the total polarization, especially in fine-grained samples with high GB densities.

In a series of studies that began in the 1990s, the atomic structural origins of these polar GBs in STO were elucidated using a combination of direct experimental techniques, including Z-contrast imaging and electron energy loss spectroscopy with a scanning transmission electron microscope (STEM), and density functional theory calculations.[15, 16] Findings from these comprehensive studies indicated that GBs in STO ceramics are inherently nonstoichiometric, with Ti:O ratios larger than the bulk values.[16] Raman and infrared spectroscopy experiments were later able to provide further evidence that such nonstoichiometry results in frozen dipole moments at GB regions, which will register as polar phases.[17]

More recently, another electron microscopy study of STO has provided new evidence for contributions from the FxE effect itself to the stable polar regions at GBs. Since GBs are interfaces with mismatched lattice parameters, by definition there must exist strain gradients at GBs. These strain gradients, and the corresponding polarizations, were quantitatively mapped out using an aberration-corrected STEM and used to estimate the FxE coefficient. The resulting FxE coefficient had good agreement with the single crystal values.[18]

Altogether, the literature suggests that polar GBs in STO should be taken into consideration when analyzing the total FxE response of polycrystalline STO. However, it remains unclear how polar GBs will respond under dynamical measurement conditions, and whether or not the frozen polarization at GBs will manifest in a macroscopic change in the polarization.

1.2.2 Point Defects and Barrier-Layer Enhancements

Closely related to polar GBs, point defects in the insulating bulk of STO ceramics might also have an important role in the total FxE response. This idea is inspired by another recent work that demonstrated orders of magnitude enhancement of the FxE effect in oxide semiconductors by doping a single crystal of $BaTiO_3$ (BTO) with oxygen vacancies via vacuum annealing.[19] This enhancement is explained according to the well-known barrier-layer dielectric model.[20]

The methods and results introduced in this recent work can potentially be used to dramatically increase the FxE effect in STO ceramics, since it is also capable of being made into a barrier-layer

capacitor. But instead of becoming a surface barrier-layer dielectric like single crystal BTO, STO ceramics have been shown to form intergranular barrier-layer dielectrics, due to the inherent differences in electrical conductivities between the GBs and the grains.[21]

1.3 Overview

The aim of this thesis is to systematically explore the effects of grain microstructure on flexoelectricity in polycrystalline materials to further understand contributions to flexoelectricity apart from the intrinsic lattice effects. Specifically, this work focused on studying how grain size affects FxE response using the model cubic perovskite STO. The key conclusions drawn from this work can provide a foundation for future studies of the FxE effect beyond ideal single crystal materials. The rest of this thesis is organized as follows. Chapter 2 introduces the experimental methods, with a specific focus on the materials processing and FxE characterization procedures. Chapter 3 presents experimental results and analyses. Chapter 4 concludes this thesis with a summary of the main findings and suggestions for future work.

Chapter 2

Experimental Methods

This chapter introduces the processing procedures and characterization techniques employed in this thesis to prepare polycrystalline STO samples and investigate their microstructural, dielectric, and FxE properties. Processing methods for obtaining bulk STO ceramics will first be described, followed by an introduction to X-ray diffraction (XRD) used for structural phase identification. Impedance spectroscopy used for measuring the dielectric constant will also be introduced. Next, a description of scanning electron microscopy (SEM) and the methods used for characterizing the ceramic grain microstructure will be provided. Lastly, the principles behind measuring the FxE response of a material will be presented.

2.1 Ceramic Sample Preparation

The approach taken for ceramic processing in this work involved compacting a fine powder into a specific shape and then heating it at an elevated temperature to achieve a dense sample. Commercially available, stoichiometric STO powder (Alfa Aesar, Ward Hill, MA) with a particle size distribution of 100-150 nm was used for all experiments. The impurity level was determined by the supplier to be less than 10,000 ppm using a metals basis.

2.1.1 Powder Pressing

The two most common procedures for compacting ceramic powders in a laboratory setting are uniaxial and isostatic pressing. The compact item produced by either of these processes is known

as a green body before sintering. Although isostatic pressing can achieve more uniform green body density, uniaxial pressing was chosen for this work given the high degree of control it provides over the shape of the green body.[22] Preparing a typical green body required inserting 0.5 g of STO into a stainless-steel die and then applying 3 US tons of force for 1 min. The resulting green body had dimensions of 30 mm x 6 mm x 1.5 mm. Experiments in this section made use of a hydraulic press (Model # 3925, Carver Inc., Wabash, IN) in Prof. Sossina Haile's laboratory at Northwestern University.

2.1.2 Sintering

The next step was to densify the green body by heating it for a period of time in a step known as sintering. For oxide ceramics, the conventional choice for this step is solid-state sintering. In this process, the difference in surface energies between a free surface and a grain boundary acts as the thermodynamic driving force for bulk diffusion. Initially, powder particles in the green body will coalesce and form necks between points and regions of contact. Grain boundaries will then form at the cross-sections of these necks, and the interstitial regions will become pores. As sintering progresses, the pores will shrink as grain growth takes place.[22] Figure 2.1.1 illustrates the different stages of solid-state sintering described above.

Numerous factors need to be considered to when sintering ceramics. These include the sintering temperature-time profile, powder packing uniformity, environmental conditions, as well as the distribution of particle sizes and shapes.[22] In this work, the same STO powder and a consistent uniaxial pressing procedure were used, and thus particle-related factors were held constant. In order to produce samples with various grain sizes, the sintering temperature was held constant while the sintering time was varied. Note, it is also possible to vary grain size by varying the sintering temperature and keeping the sintering time constant.

Figure 2.1.2 shows the sintering time-temperature profile that was used for preparing all STO samples. The sintering temperature was set at 1450 °C (limited by the maximum operating temperature of the furnace; also below the melting temperature of 2060 °C), and all samples were exposed to air during sintering. As a consequence of how the heating elements were arranged inside the furnace, a non-negligible thermal gradient existed in the vertical direction. To minimize the effects such a thermal gradient could have on sintering, the green bodies were placed on a thick alumina base plate that was resistant to warping during sintering. To prevent contamination from the alumina base plate, a thin layer of STO powder (same powder that was used to make the green bodies) was sprinkled onto the plate before placing the green bodies. Similarly, a layer

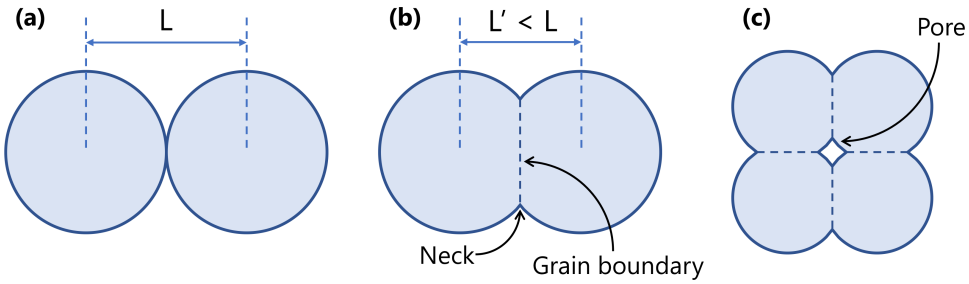

FIGURE 2.1.1. Stages of solid-state sintering. (a) Particles arrange to pack tightly. L is the center-to-center separation when assuming a spherical particle geometry. (b) A neck forms by bulk diffusion and a grain boundary emerges at the neck cross-section. The center-to-center separation (L') decreases. (c) An interstitial region becomes a pore that shrinks as sintering progresses. Grain growth occurs in both (b) and (c). Adapted from Ref. [22].

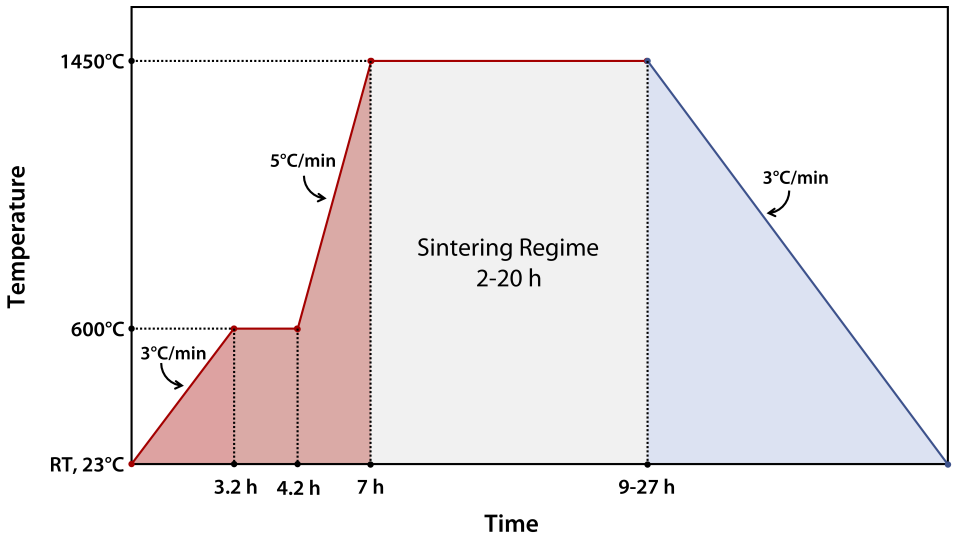

FIGURE 2.1.2. Sintering temperature-time profile. The time spent in the sintering regime (grey) was varied between 2 to 20 hours to change the grain size, with all other temperature settings unchanged. The heating regime is shaded red, and the cooling regime is shaded blue.

of STO powder was then sprinkled on top of the green bodies to minimize contamination from the furnace environment. At 1450 °C, multiple batches of samples were sintered for 2, 6, 10, 15, 18, and 20 hours. Notice in the heating regime (shaded red in Figure 2.1.2), the temperature was held at 600 °C for 1 hour in order to burn off carbonaceous contaminants. The sintered product had dimensions of approximately 25 mm x 5 mm x 1 mm. Most samples also experienced a slight degree of warpage. Experiments in this section made use of a glass melt furnace (Model # 31-THM-666-E2404, Deltech Furnaces Inc., Denver, CO) in Prof. Scott Barnett's laboratory at Northwestern University.

2.1.3 Additional Processing

Each batch of STO ceramics, typically containing 5 or 6 samples sintered for the same duration, was then separated into two groups: pristine ones used for structural and microstructural characterization (Section 2.2, 2.4), and ones that required additional processing for dielectric and FxE characterization (Section 2.3, 2.5). The additional processing involved depositing electrodes onto the samples and then attaching wires to the electrodes. Each sample was first covered by tape on one surface to leave an area of 3 mm x 10 mm exposed. A sputter coater was then used to deposit approximately 50 nm of gold onto the exposed area to form an electrode. The same procedure was then carried out for the opposite surface. Next, a copper wire was attached to each of the electrodes with silver paste, and the entire sample was heated at 300 °C for 3 hours to ensure electrical conductivity between the wires and the electrodes, as well as mechanical stability at the attachment points. Experiments in this section made use of a sputter coater (Desk IV, Denton Vacuum LLC, Moorestown, NJ) in the Electron Probe Instrumentation Center, and a box furnace (Lindberg Blue M 5.3 L, Thermo Scientific, Waltham, MA) in Prof. Kenneth Poeppelmeier's laboratory at Northwestern University.

2.2 X-Ray Diffraction

XRD is a powerful technique for studying the structure of materials, and is widely used for crystal structure determination and to assist in phase identification.[23] In principle, XRD utilizes elastic scattering of X-rays from a material to produce a diffraction pattern that can provide insight into the atomic arrangement of the material, i.e. its crystal structure. Experimental diffraction patterns can be compared to standard diffraction patterns from well-curated databases, thus enabling unique identification of a material's structural phase. In a diffraction pattern, two prominent features to note are the diffraction peak locations and intensities. The angular locations of diffraction peaks are governed by Bragg's Law:

$$\lambda = 2d_{hkl} \sin \theta \tag{2.2.1}$$

where λ is the wavelength of the incident X-ray, d_{hkl} is the interplanar spacing between (hkl) planes, and θ is the angle of incidence relative to the sample for maximum constructive interference. Each peak location (2θ) can be converted by Bragg's law into a d_{hkl} value that is independent

of the experimental settings. This information can then be used to find unit cell dimensions of a crystal from its diffraction pattern in a process known as refinement.[23] On the other hand, diffraction peak intensities reveal information about the structure within a unit cell, such as the types of atoms present and their positions. Since absolute intensities may vary with experimental parameters, it is typically more beneficial to compare the relative (or normalized) intensities of diffraction peaks.

2.2.1 Powder Method X-Ray Diffraction

There are three common implementations of XRD depending on both the diffraction geometry and the X-ray source: the Laue, rotating crystal, and powder methods. The Laue and rotating crystal methods are ideal for studying single-crystalline samples, while the powder method is suitable for polycrystalline samples, such as the STO ceramics studied in this work.[23] Polycrystalline samples are assumed to contain a statistically significant number of crystallites in all crystallographic orientations, such that Bragg's law is satisfied for each orientation, resulting in diffraction patterns that contains all possible diffraction peaks. In this work, pristine polycrystalline STO samples were irradiated by a Cu-$K\alpha$ X-ray source using an X-ray diffractometer setup in the Bragg-Brentano para-focusing geometry.[23] The incident beam was limited by a divergence slit width of 1/2 °. Diffraction patterns were acquired with a step size of 0.03 °. XRD experiments made use of an X-ray diffractometer (Ultima III, Rigaku Corporation, Tokyo, Japan) in the Jerome B. Cohen X-Ray Diffraction Facility at Northwestern University.

2.3 Impedance Spectroscopy

Impedance spectroscopy represents a family of methods for characterizing electrical properties of materials, especially the dielectric and electrochemical behaviors of solids.[24] In practice, impedance spectroscopy commonly involves applying an AC voltage to a sample with a well-defined geometry (usually a pellet or bar) and detecting both the amplitude and the phase shift in the current response. This information can be used to obtain the impedance Z of the sample, which is defined as:

$$Z = \frac{|V|e^{j(\omega t+\phi_V)}}{|I|e^{j(\omega t+\phi_I)}} \tag{2.3.1}$$

where $|V|$ and $|I|$ are the magnitudes of the AC voltage and current signals, respectively, ω is the radial frequency, t is time, ϕ_V and ϕ_I are the phase shifts in the AC voltage and current signals, respectively. Equation 2.3.1 implicitly defines the impedance of the sample as a function of the frequency of the applied AC voltage. Common electrical properties, such as resistance, capacitance, and inductance, etc., have distinct frequency responses, and can be determined by measuring the impedance over a wide range of frequencies.

2.3.1 Dielectric Constant Measurement

In this work, impedance spectroscopy was used to find the dielectric constant, also known as the relative permittivity, of the STO ceramic samples. The approach taken was to measure each sample's capacitance and then solve for its dielectric constant by modelling the sample as a parallel plate capacitor. The details of this analysis method are described in Section 3.3. The amplitude of the AC voltage was set to a default value of 100 mV, while the frequency of the AC voltage was swept from 1 kHz to 1 MHz during the measurements. Experiments in this section made use of an impedance analyzer (Model # 1260, Solartron Analytical, Hampshire, United Kingdom) in the Materials Characterization and Imaging Facility at Northwestern University.

2.4 Scanning Electron Microscopy

SEM is an analytical tool routinely used for studying the microstructure of materials at the nanometer to micrometer length scales. The main utility of SEM lies in its ability to generate images with high spatial resolution and high depth-of-field, qualities difficult to achieve with traditional optical microscopy methods. Apart from imaging, SEM can also provide information of the chemical composition of a material. During SEM operation, a focused beam of high-energy electrons (typical energies of 10-30 keV) is raster scanned across the sample, and the electron beam-sample interaction produces various sources of radiation, such as secondary electrons, backscattered electrons, X-ray photons, and visible light. These radiation signals can be collected by specialized detectors equipped on the microscope, and reveal information of different aspects of the sample.[25]

For imaging a sample's microstructure, a common choice is to use secondary electrons, which result from the process of high-energy electrons inelastically scattering from features of the sample. The short inelastic mean free path of secondary electrons renders them highly sensitive to surface morphology, such as slight corners and edges on otherwise smooth surfaces.[25] Secondary

electron imaging is therefore able to provide information about the exposed microstructure of a material, which can be later used in qualitative or quantitative analyses.

2.4.1 Grain Size Measurement

In this work, SEM was used to obtain secondary electron images of the microstructures of the STO samples for grain size measurements. Pristine STO ceramics from each batch (different than the ones used for XRD) were sputter coated with approximately 50 nm of gold to prevent charging effects during imaging. While it is desirable to first mechanically polish the surface of the sample before imaging to determine the average grain size, this procedure was omitted due to the severe grain pullout the samples experienced even under mild polishing conditions. The accelerating voltage of the SEM was set at 20 kV for all experiments. Images of different regions of each sample were then acquired at magnifications ranging from 1500X to 10000X depending on the grain size. The average grain size was measured from these images using the lineal intercept method.[26] This procedure required drawing 5 straight lines each at 0 °, 45 °, 90 °, and 135 ° across every image, and counting the number of intersections between the lines and the grain boundaries. Triple boundaries were counted as 1.5 intersections. This process was carried out using FIJI, a specific distribution of the ImageJ software.[27] The total length of the lines was then divided by the total number of intersections to obtain an average intercept length. This average intercept length was then scaled by a constant geometric factor of 1.56 to find the average grain size in three-dimensions.[28] Experiments in this section made use of an SEM (Quanta 650 ESEM, FEI Company, Hillsboro, OR) and a sputter coater (Desk IV, Denton Vacuum LLC, Moorestown, NJ) in the Electron Probe Instrumentation Center at Northwestern University.

2.5 Flexoelectric Characterization

In Section 1.1, it was shown that the FxE properties of a material are fully characterized by its FxE coefficients. In practice, FxE coefficients can be determined via the direct FxE effect by applying a strain gradient and measuring the polarization response. The overall strategy is to collect polarization values for different strain gradients. The linear fit obtained from this data will be a linear combination of the sample's FxE coefficient tensor components. The exact linear combination that is measured is a function of the sample's crystal structure, crystallographic orientation, and geometry of the measurement. The description of the FxE characterization procedure in this section closely follows Ref. [29]

In general, carrying out a FxE measurement via the direct effect requires overcoming two key experimental challenges. The first challenge lies in delivering a small strain gradient in a controlled fashion. If the strain gradient is too large it may cause irreversible deformation to the sample, such as permanently breaking centrosymmetry, which may then induce a piezoelectric response in an otherwise non-piezoelectric material.[30] An intuitive way of generating a strain gradient is through bending. As described in Ref. [14], one way to controllably bend a sample is by a dynamic mechanical analyzer (DMA) with the sample in a three-point bending (TPB) configuration. The profile view of a sample setup in a TPB configuration is shown in Figure 2.5.1 (a), and the corresponding strain gradient developed in the sample is shown in Figure 2.5.1 (b). The DMA can control precisely how far the top knife edge is brought down onto the sample, and therefore achieve control of the magnitude of the applied strain gradient.

The second challenge lies in measuring small polarizations. This is due to the fact most materials have FxE coefficients on the order of nC/m to μC/m, which means that the small applied strain gradients, typically on the order of 0.01 to 0.1 1/m, will only be able to generate small polarizations on the order of pC/m^2 to nC/m^2.[3] In practice, these small polarizations are measured as current signals on the order of pA to nA. The difficulty of this problem is alleviated by the fact that using a DMA, the applied strain gradients are oscillatory by default. Therefore, the current signals that develop via the direct FxE effect are also oscillatory and at the same frequency as the applied strain gradient. This permits measurement of small current signals against a noisy background using a lock-in amplifier (LIA). The next two subsections will describe the mechanical and electrical aspects of performing FxE measurements.

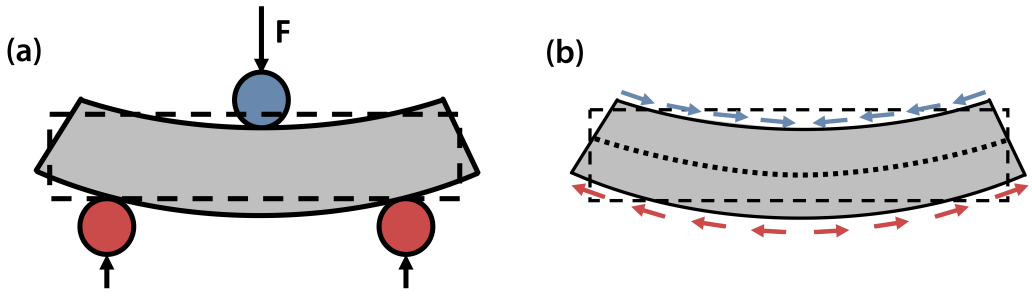

FIGURE 2.5.1. TPB configuration setup with a DMA. (a) Profile view of the bent sample (grey) supported at two regions of contact (red) and pinned down by a knife edge (blue) at a certain force F. The sample is initially at the position of the dashed lines. (b) Profile view of the strain gradient developed from the setup in (a). The top surface of the sample is under compressive strain (blue arrows), while the bottom surface is under tensile strain (red arrows). The dotted line through the center of the bent sample represents the neutral plane where the strain is 0. Adapted from Ref. [29].

2.5.1 Mechanical Data Collection

The mechanical aspect of FxE characterization involved using a DMA to deliver an oscillatory strain gradient as described above to the STO samples. DMAs are widely used for measuring macroscopic mechanical properties of solids, and especially polymeric materials.[31] A DMA functions by applying a mechanical stimulus to a material in a well-defined geometry and measuring the resulting mechanical responses, such as storage and loss moduli. STO samples with electrodes and wires attached to either side were used for all FxE measurements. The dimensions of these samples are all approximately 25 mm x 5 mm x 1 mm, as described in Section 2.1.2. For the case of a sample in a TPB configuration, the relation between the applied oscillatory force f at the center of the sample and the resulting displacement u can be expressed as:

$$\frac{f}{u} = Y 4b \left(\frac{h}{L}\right)^3 \left[1 + \frac{3}{2}\left(\frac{h}{L}\right)^3 \frac{Y}{G}\right]^{-1} \tag{2.5.1}$$

where Y is the storage modulus along the direction of the sample length, b is the sample width, h is the sample thickness, L is the distance between the bottom supports, and G is the shear modulus.[32] In the limit of a thin beam, which applies to the STO samples, the term containing G can be dropped and Equation 2.5.1 can be rearranged with Y on the l.h.s. and measurable quantities on the r.h.s.:

$$Y = \frac{f}{4bu}\left(\frac{L}{h}\right)^3 \tag{2.5.2}$$

Equation 2.5.2 can then be used to calculate the strain gradient along the z direction of the sample from Euler-Bernoulli theory.[33]. This gives the result:

$$\frac{\partial \epsilon(x)}{\partial z} = 6\frac{f}{Ybh^3}\left(\frac{L}{2} - x\right) \tag{2.5.3}$$

where x is along the direction of the sample length (and electrode length). The strain gradient in Equation 2.5.3 is a function of the x coordinate, and x is set to 0 at the center of the sample. As discussed later, because the polarization response can only be determined over the area of the electrode, the average strain gradient across the length of the electrode also needs to calculated. The result can be expressed as:

$$\overline{\frac{\partial \epsilon}{\partial z}} = \frac{1}{a}\int_0^a \frac{\partial \epsilon(x)}{\partial z} dx = 3\frac{f}{Yh^3}\frac{L-a}{b} \tag{2.5.4}$$

where a is half of the length of the electrode. As shown in Equation 2.5.4, the magnitude of the average strain gradient can be varied by changing the magnitude of the applied oscillatory force. Typically, at least 5 different strain gradients levels were tested for each sample. The frequency of all the oscillatory forces were fixed at 33 Hz for reasons that will be described in the next subsection. It is important to note here that in addition to the oscillatory force, a fixed static force (greater than the oscillatory force) was first applied to the sample to maintain contact during the experiment and prevent any lateral movement that can disrupt the experiment. The static force was set to be approximately 1.5 N. Experiments in this section made us of a new DMA (RSA-G2, TA Instruments, New Castle, DE) in the Materials Characterization and Imaging Facility, and an older DMA (RSA III, TA Instruments, New Castle, DE) in Prof. Kenneth Shull's laboratory at Northwestern University.

2.5.2 Electrical Data Collection

The electrical aspect of FxE characterization involved simultaneously using the LIA to detect current signals from STO samples that underwent oscillatory bending experiments in the DMA. LIAs are widely used for extracting and amplifying a specific component of a signal, with a known frequency and phase, from noisy environments and rejecting all other components of that signal. This is achieved by a technique known as phase-sensitive detection.[34] In practice, the wires of each STO sample were connected to the input terminals of the LIA, and the DMA was also connected to a reference terminal of the LIA. During measurements, a reference signal with the same frequency (33 Hz) and phase as the oscillatory force signal was supplied from the DMA, and the LIA was programmed to select out the desired components of the current signal that matched this frequency and phase. The frequency of 33Hz was chosen to prevent power-line frequency interference with the locked-in signal. For each STO sample, the average polarization in the z-direction can then be calculated using the expression:

$$\left|\overline{P_z}\right| = \frac{I/2}{\omega A} \tag{2.5.5}$$

where $|P_z|$ is the magnitude of the polarization in the z-direction, I is the measured current, ω is the radial frequency (set to 33 Hz for all measurements), and A is the average area of the electrode.

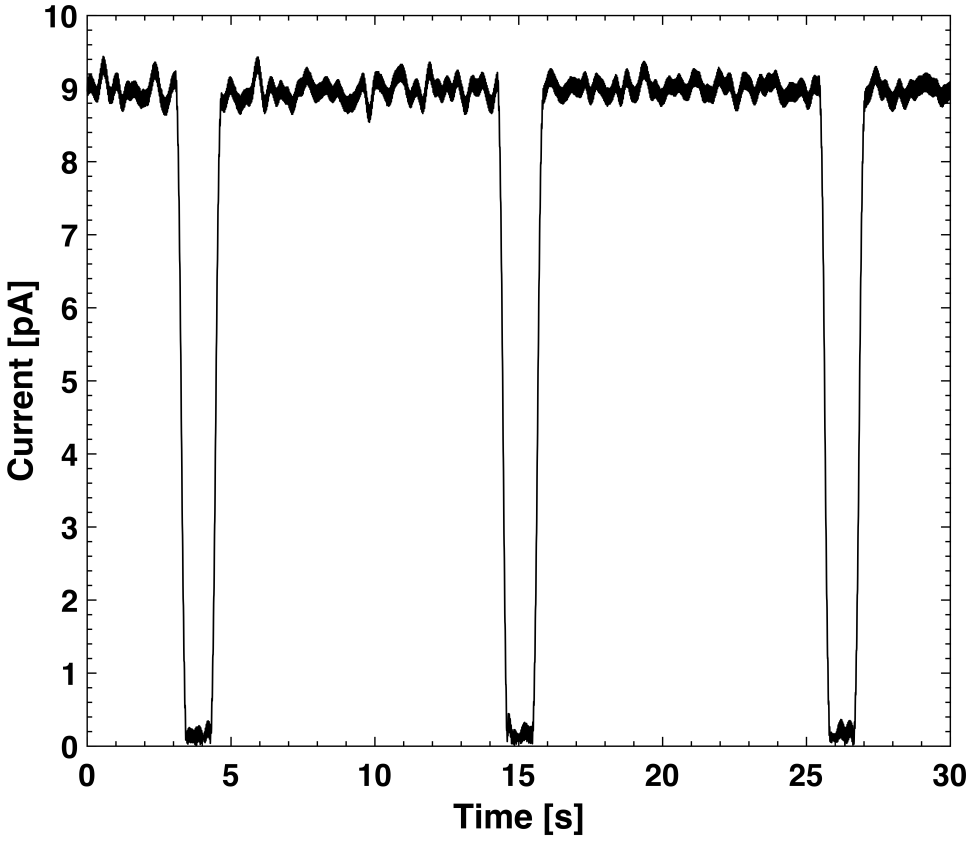

FIGURE 2.5.2. Example current acquisition result using the LIA. The average current here is approximately 9 pA, and the total average current is the average over 5 of such current acquisitions.

This equation implicitly indicates that the polarization is an average over the entire electrode area. This is the reason why the strain gradient needed to be averaged in the previous section. An example result of one current acquisition with the LIA at a fixed strain gradient is shown in Figure 2.5.2. Since the DMA that was used can only operate in discrete intervals, the resulting current is discontinuous as shown. In order to improve the precision of current measurements (and therefore the average polarization measurements), typically 5 current acquisitions were obtained for each strain gradient level and then averaged. Experiments in this section made us of two LIAs of the same kind (Model # 7265, Signal Recovery, Oak Ridge, TN) in Prof. Laurence Marks' laboratory and Prof. Lincoln Lauhon's laboratory at Northwestern University.

Chapter 3

Results and Discussion

3.1 Powder Method XRD Measurements

Powder method XRD was employed to verify the crystal structure of STO ceramics. All samples were prepared following the methods described in Section 2. The measured diffraction patterns for the 2, 6, 10, 15, and 20-hour samples are indicated in Figure X, along with a standard diffraction pattern of cubic STO.[35] There is good agreement between all the experimental diffraction patterns and the target cubic STO crystal structure. Additionally, within experimental resolution there is no indication of the presence of secondary phases in these samples. Furthermore, comparison of the relative peak intensities within each diffraction pattern to relative peak intensities of the standard diffraction pattern shows that there is no apparent texture in any sample. All of the expected peaks are visible in each experimental diffraction pattern, and there are no abnormal peak intensities. It is also worth noting that peak splitting occurs, and is likely a consequence of the X-ray beam containing both Cu-Kα 1 and Cu-Kα 2 radiation. This is demonstrated by the fact that this effect is more prominent at high angles. Peak splitting, however, does not affect the results interpretation discussed above. Finally, it is noted that there is a significant shoulder on the left side of the first peak in the 20-hour sample, as well as low intensity features between 24 $^\circ$ and 30 $^\circ$. The origins of these features are unknown and might indicate contamination.

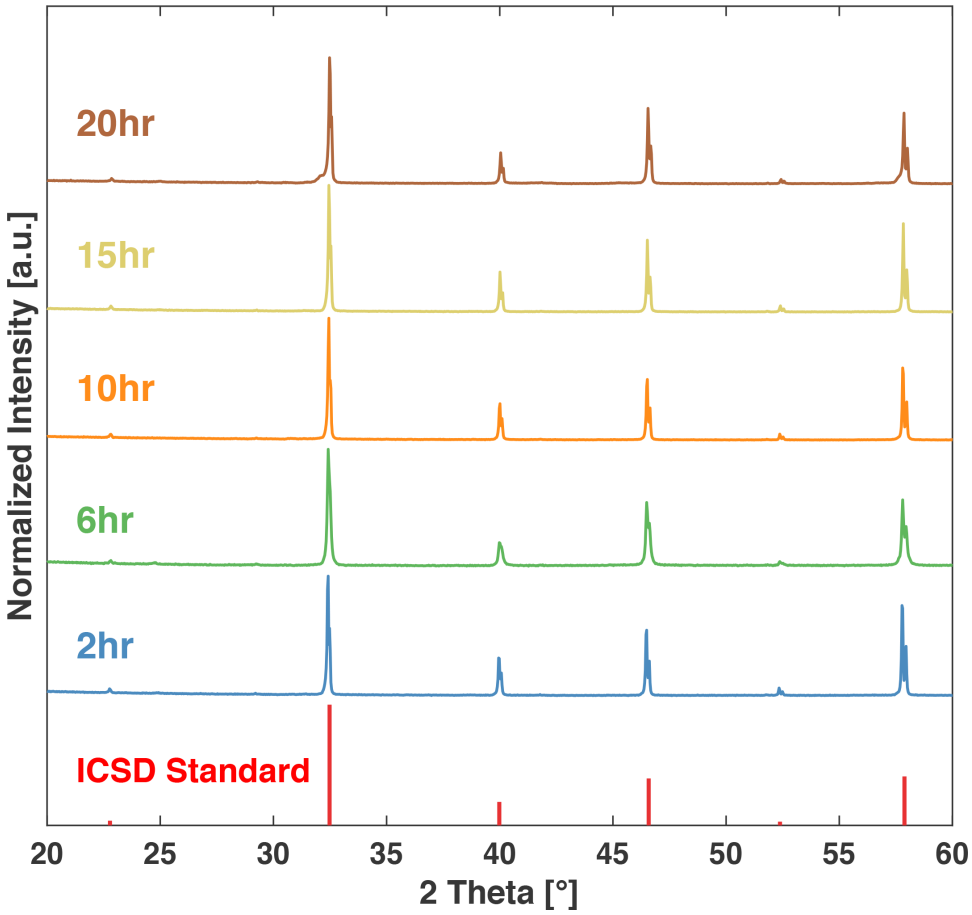

FIGURE 3.1.1. Experimental results of X-ray diffraction patterns of STO ceramics. The bottom diffraction pattern (red) represents a high-quality cubic STO standard.[35] The measured diffraction patterns for samples sintered for various times are in good agreement with the cubic STO crystal structure and do not indicate the presence of any secondary phases.

3.2 Average Grain Size Measurements

Average grain size is considered a characteristic parameter when describing the microstructure of polycrystalline materials. For the purpose of this work, it was important to quantify the average grain size of the STO ceramics with high precision following the procedure in Section 2.4.1. The measured average grain sizes for the 2, 6, 10, 15, 18, and 20-hour samples are plotted in Figure 3.2.1. Table 3.1 lists the average grain size values with their associated standard errors. Because the procedure in Section 2.4.1 does not permit measurement of grain size distributions, and thus error estimations, the errors here were determined by binning the measurements based on the images they came from. At least 5 images were acquired for each sample. Representative secondary electron images of the microstructure of the 2-hour and 20-hour samples are shown in Figure 3.2.1 (b) and (c), respectively. These images show the two extremes in the average grain sizes.

As expected, there is an overall increase in the average grain size of the STO ceramics from 2.08 ± 0.1 μm to 11.41 ± 0.8 μm as the sintering time is increased from a minimum of 2 hours to a maximum of 20 hours (while the temperature was held at 1450 °C). However, the sample sintered for 15 hours deviates from this trend, and has an average grain size of 4.54 ± 0.3 μm, significantly lower than the average grain size of 5.88 ± 0.1 μm for the sample sintered for 10 hours. While it is possible that the average grain size in the 15-hour sample was smaller than 10-hour sample, it is more likely that the regions selected for grain size measurements on the 15-hour sample might not be accurate representations of the sample's microstructure. Since the sintering time and the grain size are generally well-correlated, sintering time is used as a proxy for the average grain size in all subsequent discussions.

TABLE 3.1. Average grain sizes and associated standard errors of STO ceramics sintered at 1450 °C

Sample	Average Grain Size [μm]
2-hour	2.08 ± 0.1
6-hour	5.54 ± 0.5
10-hour	5.88 ± 0.1
15-hour	4.54 ± 0.3
18-hour	7.76 ± 0.4
20-hour	11.41 ± 0.8

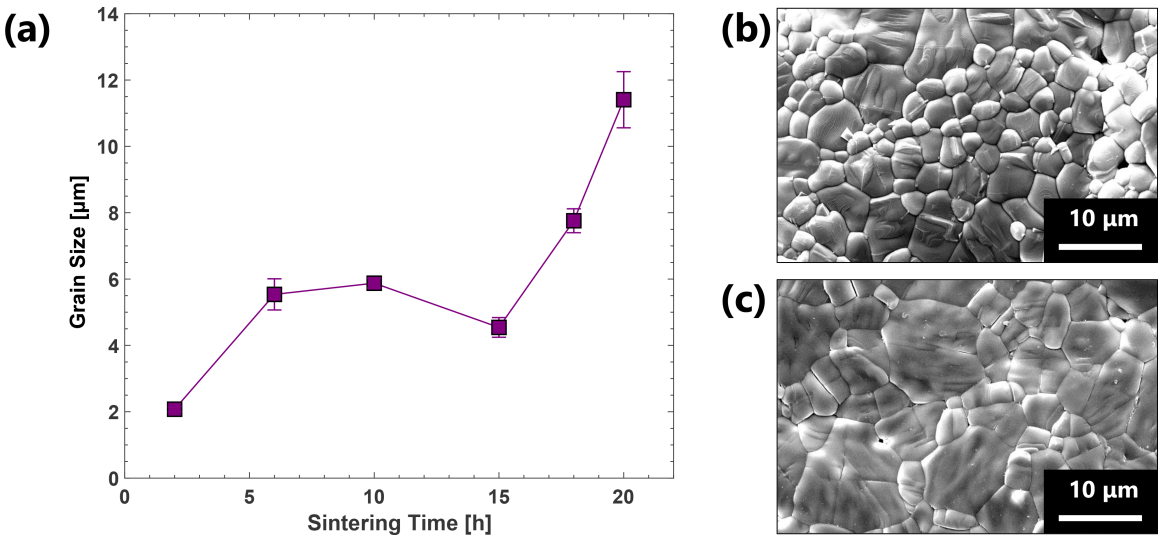

FIGURE 3.2.1. Experimental results of average grain size measurements of STO ceramics sintered at 1450 °C. (a) Average grain size increases from 2.08 ± 0.1 μm to 11.41 ± 0.8 μm as the sintering time increases from 2 hours to 20 hours. The average grain size of the 15-hour sample deviates from this trend and is potentially due to insufficient sampling. The error bars correspond to the standard error listed in Table 3.1. Secondary electron image of (a) ceramic sample sintered for 2 hours, and (b) ceramic sample sintered for 20 hours.

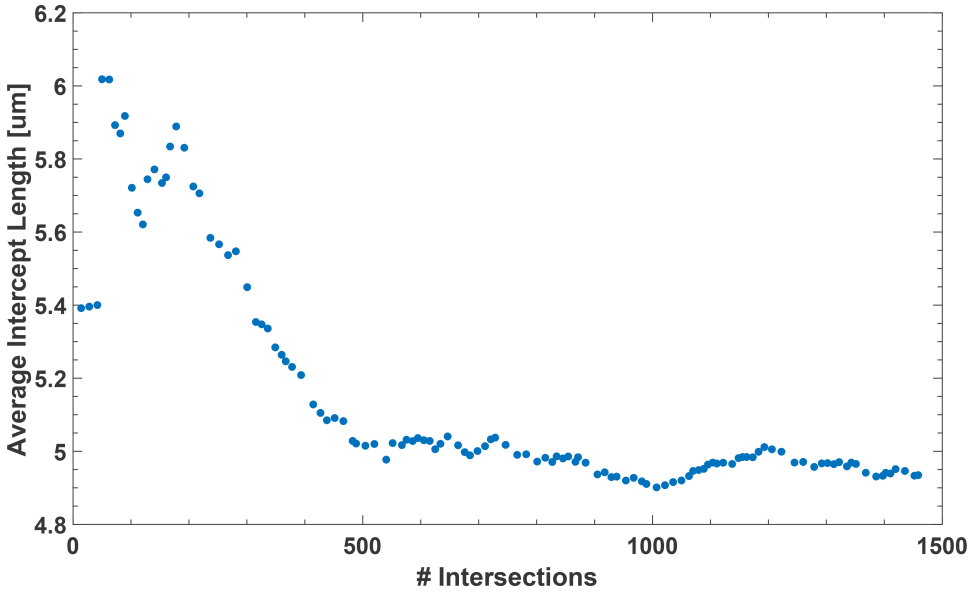

FIGURE 3.2.2. Example of grain size counting results. The data represents counting over 5 images taken from different regions of an STO ceramic sintered for 18 hours. The average intercept length varies as more grains are counted and finally reaches a converged value. In this example, a total of 1458.5 intersections were counted and the final value is 4.93 μm. Note: this final value is only the average intercept length value, which is different from the average grain size.

An example of the procedure for obtaining the final average intercept length (and thus the average grain size) is shown in Figure 3.2.2. During counting, the average intercept length was updated as more intersections (more grains) were included and reached a final converged value from observation. Typically, this process required approximately 1500 counts for each sample.

3.3 Dielectric Constant Measurements

Dielectric constant measurements of the STO samples were required to determine their FcVs, which can provide a convenient measure of the magnitude of the FxE response across different materials.[3] The experimental procedure for finding the dielectric constant with impedance spectroscopy is described in Section 2.3, and the analysis involves first finding the relation between the impedance and frequency for an ideal capacitor. This relation can be derived by considering the constitutive equation for a capacitor:

$$I(t) = C\frac{\mathrm{d}V(t)}{\mathrm{d}t} \tag{3.3.1}$$

where I is the current through the capacitor, V is the voltage across the capacitor, and C is the capacitance. For an AC voltage signal, $V(t)$ takes the form:

$$V(t) = |V|e^{j(\omega t+\phi_V)} \tag{3.3.2}$$

where again $|V|$ is the magnitudes of the AC voltage, ω is the radial frequency, and ϕ_V is the phase shift. The current response of the capacitor $I(t)$ can therefore be written as:

$$I(t) = C\frac{\mathrm{d}V(t)}{\mathrm{d}t} = j\omega C|V|e^{j(\omega t+\phi_V)} \tag{3.3.3}$$

Equation 3.3.2 and Equation 3.3.3 combine to give the impedance of a capacitor:

$$Z = \frac{|V|e^{j(\omega t+\phi_V)}}{j\omega C|V|e^{j(\omega t+\phi_V)}} = \frac{1}{j\omega C} \tag{3.3.4}$$

Equation 3.3.4 indicates that the impedance of an ideal capacitor is purely imaginary, and its magnitude is inversely proportional to the radial frequency. The magnitude of the impedance can be plotted against the inverse of the radial frequency, and the slope of the linear fit will give the inverse of the capacitance. Assuming that the sample can be modelled by a parallel-plate capacitor, the dielectric constant ϵ_r of the sample can thus be determined from its capacitance:

$$\epsilon_r = \frac{Cd}{A\epsilon_0} \tag{3.3.5}$$

where d is the thickness of the sample, A is the electrode area, and ϵ_0 is the permittivity of free space. To benchmark the analysis method described above, impedance spectroscopy experiments were first carried out at room temperature on a (100) oriented MgO single crystal sample (MTI Corporation, Richmond, CA), which has an extensively measured dielectric constant.[36] 50 nm thick gold electrodes were sputtered on either side of the MgO single crystal, and the average area of the electrodes were determined to be 1.74×10^{-5} m^2 (measured from optical images using FIJI). The MgO sample has a thickness of 0.5 mm (provided by the supplier). The results for this experiment are shown in Figure 3.3.1 (a), and the fitted line is shown to be a good representation of this data, with an R^2 value exceeding 0.99. The capacitance of this sample is determined to be 3.03 pF, and the dielectric constant of this MgO sample is determined to be 9.84, which is in excellent agreement with the literature value of 9.83 at 300 K.[36]

This analysis method was then applied to impedance data collected on STO samples sintered for 2, 10, 15, 18, and 20 hours, and the results are shown in Figure 3.3.1 (b). Overall, the dielectric constants of the samples are spread around the dielectric constant of a (100) oriented single crystal STO, which has a value of 330.[37] Although the dielectric constants do not indicate a distinct trend with the sintering time, their magnitudes are slightly different, and this fact becomes important later. It is possible that the differences in dielectric constant reflect the underlying porosity of the ceramics; future work is required to explore this hypothesis.

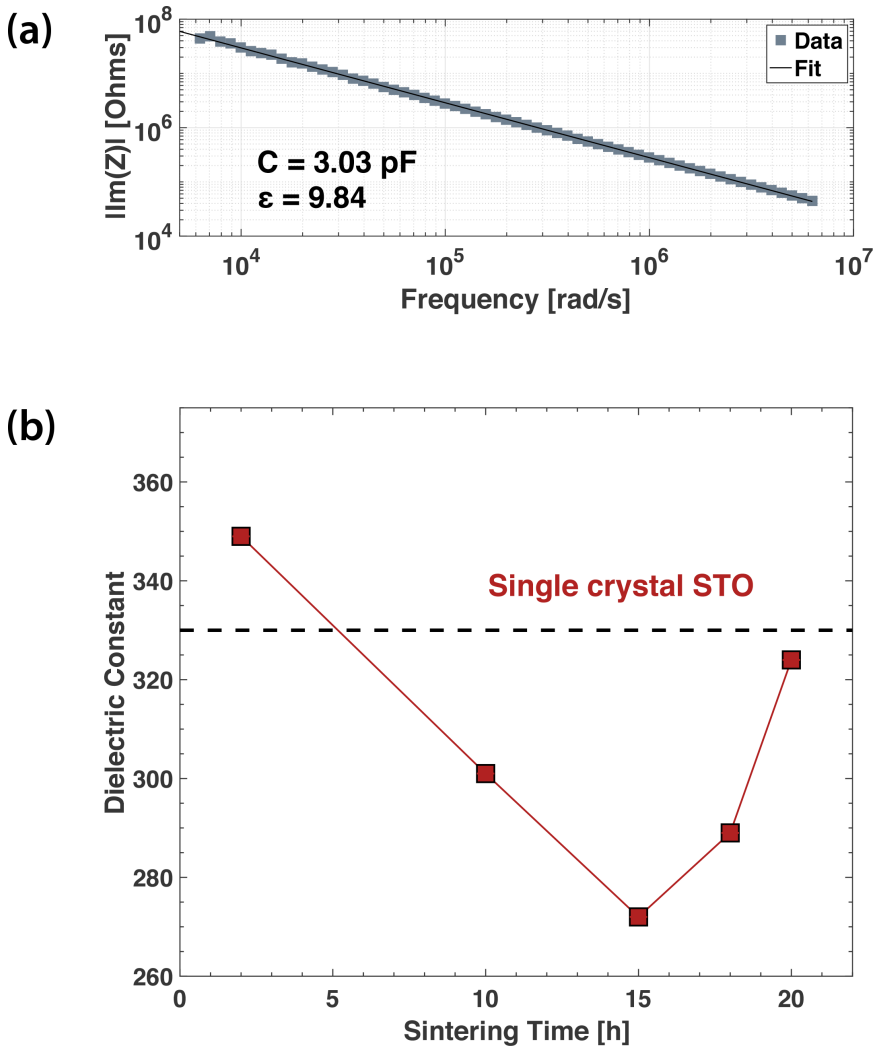

FIGURE 3.3.1. Experimental results for impedance spectroscopy measurement of an MgO test sample and various STO samples. (a) Impedance versus frequency measured for an MgO (100) single crystal. The measured dielectric constant for MgO is in close agreement with the literature value, validating the measurement procedure.[36] (b) Dielectric constants of STO samples sintered for various times. The dielectric constants of the polycrystalline STO samples are spread around the single crystal STO value of 330, showing no distinct trend with the sintering time, and by extension the grain size.[37]

3.4 FxE Characterization Results

FxE characterization was performed on the 2, 10, 15, 18, and 20-hour STO samples using the instrument system and procedure described in Section 2.5. The results of individual measurements are shown in Figure 3.4.1, while the values of the FxE coefficients and their associated errors are listed in Table 3.2. Errors are given by the 95% confidence interval of the linear fit to each sample's data set. These linear fits are shown as dashed lines in Figure 3.4.1. The linear fits are of high quality, with R^2 values exceeding 0.95 for all samples.

It can be seen from Figure 3.4.1 that there is a substantial difference between the FxE coefficients of the STO samples sintered for various times. A maximum FxE coefficient of 42.20 ± 1.6 nC/m was achieved for the 10-hour sample, while a minimum FxE coefficient of 4.26 ± 0.3 nC/m was found for the 20-hour sample. It also worth noting that the coefficients of the 2-hour and 10-hour samples are not distinguishable within experimental resolution. In order to more clearly observe variations in the FxE coefficients, Figure 3.4.2 was rendered to show only the FxE coefficients plotted against the sintering time. This result directly indicates that the STO samples with short sintering times (2, 10, and 15 hours) have FxE coefficients that are approximately an order of magnitude greater those of samples with longer sintering times (18 and 20 hours). In addition, at longer sintering times, the FxE coefficients of the polycrystalline ceramics are comparable to the single crystal STO FxE coefficients, which have been measured to be in the range of 1 nC/m to 10 nC/m.[14, 38]

TABLE 3.2. FxE coefficients and associated errors of STO samples. All errors correspond to the 95% confidence interval of the linear fits.

Sample	FxE Coefficient [nC/m]
2-hour	38.43 ± 4.1
10-hour	42.20 ± 1.6
15-hour	29.76 ± 2.3
18-hour	5.92 ± 1.3
20-hour	4.26 ± 0.3

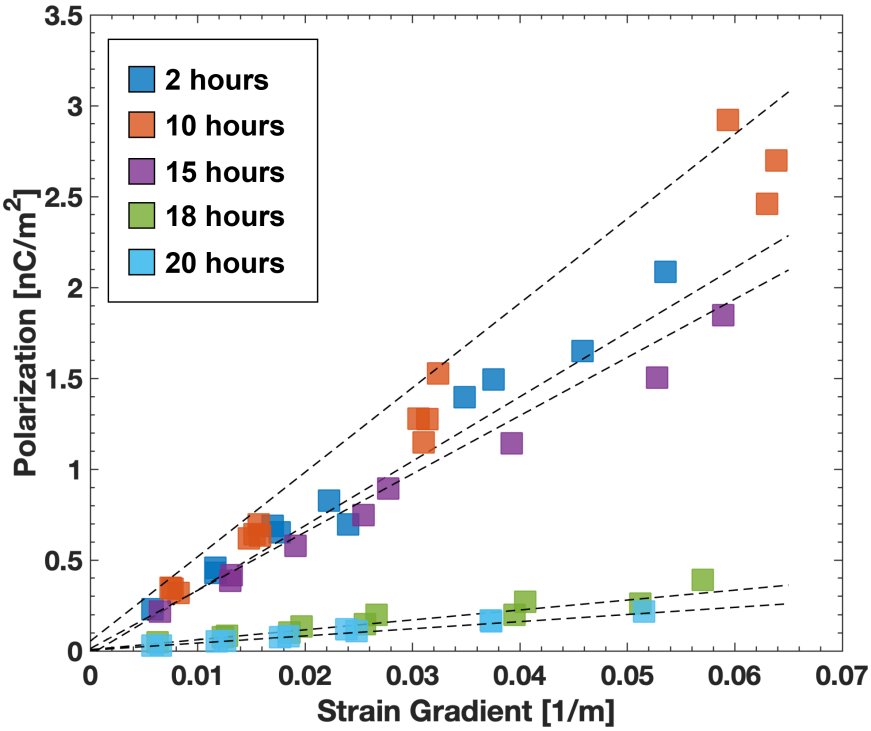

FIGURE 3.4.1. Experimental results of FxE coefficient measurements for various STO samples. The dashed lines represent linear fits to the experimental data, with R^2 values exceeding 0.95 for all samples. The slopes of the fitted lines are the FxE coefficients.

As described in the Section 1.2, the measured FxE coefficient represents the total FxE response of the sample. In a polycrystalline material system, the total FxE response can be considered as the result of three different contributions, the lattice FxE term (e.g. bulk lattice in each grain), pseudo FxE terms (e.g. polar grain boundaries and point defects), and FxE low activity or inactive terms (e.g. grain boundary sliding, dislocation motion etc.). To first order, the FxE low activity terms can be ignored so that the total FxE response in STO samples consists only of lattice FxE and pseudo FxE terms. During sintering and grain growth, two main microstructural effects will occur: (1) The total grain boundary volume decreases as sintering time increases (and grains grow larger). It is expected that the pseudo FxE term is directly proportional to the total grain boundary volume. Therefore, at longer sintering times, the total FxE response should decrease and approach that of the bulk lattice. (2) The point defect concentration is likely reduced with increasing sintering time. Although the implications of this second effect happening should be explored, they are not the central focus of this work. The experiment results shown in Figure 3.4.2 thus provide direct evidence to support the claim that the first effect is present in this work.

Another way to quantify the FxE response is in terms of the FcV, which takes into account differences in the dielectric constant. The FcV, as defined in Section 1.1 is the ratio of the FxE coefficient

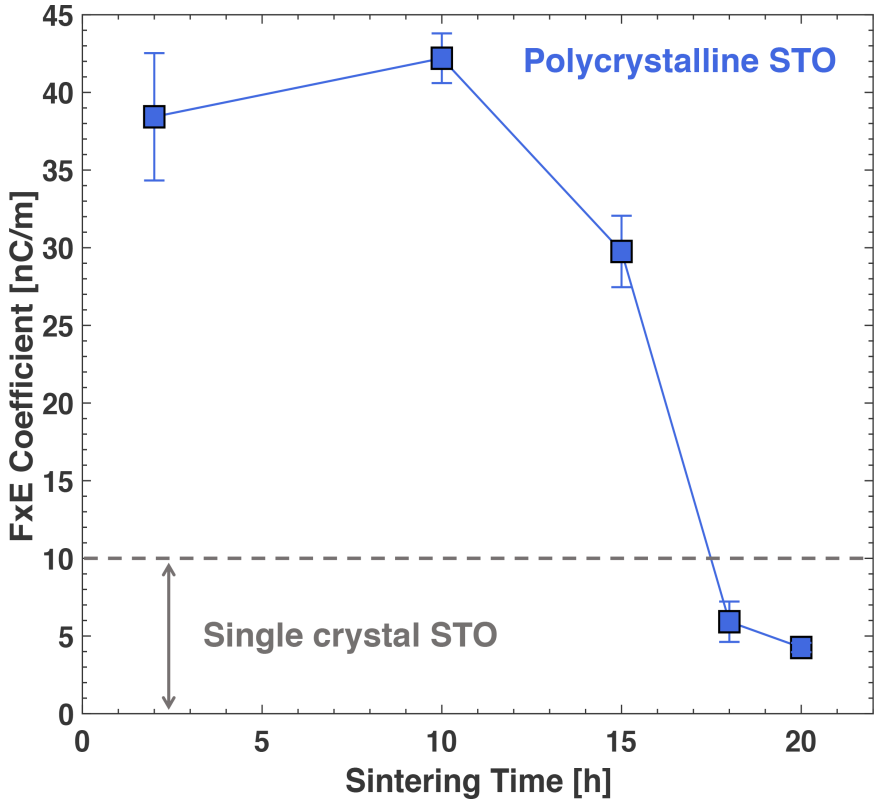

FIGURE 3.4.2. Experimental results of FxE coefficients of various STO samples plotted against sintering time. FxE coefficients of the STO samples vary with the sintering time; samples sintered for relatively short times have FxE coefficients nearly an order of magnitude greater than those of samples sintered for long times. The grey double arrow and dotted line indicate the range of experimental FxE coefficients reported in literature for STO single crystals.[14, 38]

to the susceptibility, which is the product of the dielectric constant and the permittivity of free space. This definition provides a convenient way to compare the magnitude of the direct FxE effect to the magnitude of an electric field in dielectric materials. This can be shown by examining the one-dimensional bulk constitutive electromechanical equation for a centrosymmetric material:

$$P = \chi E_{applied} + \mu \frac{\partial \varepsilon}{\partial \mathrm{x}} \tag{3.4.1}$$

where P is the polarization, χ is the susceptibility (product of dielectric constant and permittivity of free space), $E_{applied}$ is the applied electric field, μ is the FxE coefficient, and $\partial\epsilon/\partial x$ is the strain gradient. Dividing both sides of this equation by the susceptibility, and assuming that there is no applied field, the l.h.s turns into an effective electric field, which is equal to the r.h.s, which turns into the product of the FcV and the strain gradient:

$$E_{effecttive} = f\frac{\partial \epsilon}{\partial x} \tag{3.4.2}$$

The FcVs of the STO samples sintered for 2, 10, 15, 18, and 20 hours were calculated using the dielectric constant measurements from Section 3.3, and these results are shown in Figure 3.4.3. The FcV, similar to the FxE coefficients, displays an order of magnitude decrease as the sintering time increases, with the variation in the dielectric constant not appearing to affect the overall trend. In addition, the measured FcVs can be compared to the theoretical upper limit of 10 V for a simple ionic material, which is shown as the horizontal dashed line in Figure 3.4.3.[3, 11] The samples sintered for 2, 10, and 15 hours have flexocoupling voltages that exceed this upper limit, providing further evidence for contributions other than the lattice response to the total FxE effect.

However, in an attempt to repeat these FxE measurements with the same samples, an interesting observation was made. The FxE coefficients of the same 2, 10, 15, and 18-hour samples measured for a second time, two months later, were all significantly lower than they were in the initial measurements. The measured coefficients are shown in Figure 3.4.4 plotted against the sintering time. Table 3.3 lists the values of the FxE coefficients and their associated errors, which were determined in the same way as before. The FxE coefficients for samples sintered for all the different times decreased by more than a factor of 10, and the original trend in the FxE coefficient with sintering time is no longer observed.

TABLE 3.3. FxE coefficients and associated errors of STO samples measured for a second time. All errors correspond to the 95% confidence interval of the linear fits.

Sample	FxE Coefficient [nC/m]
2-hour	2.12 ± 0.4
10-hour	1.65 ± 0.2
15-hour	2.41 ± 0.1
18-hour	0.48 ± 0.1

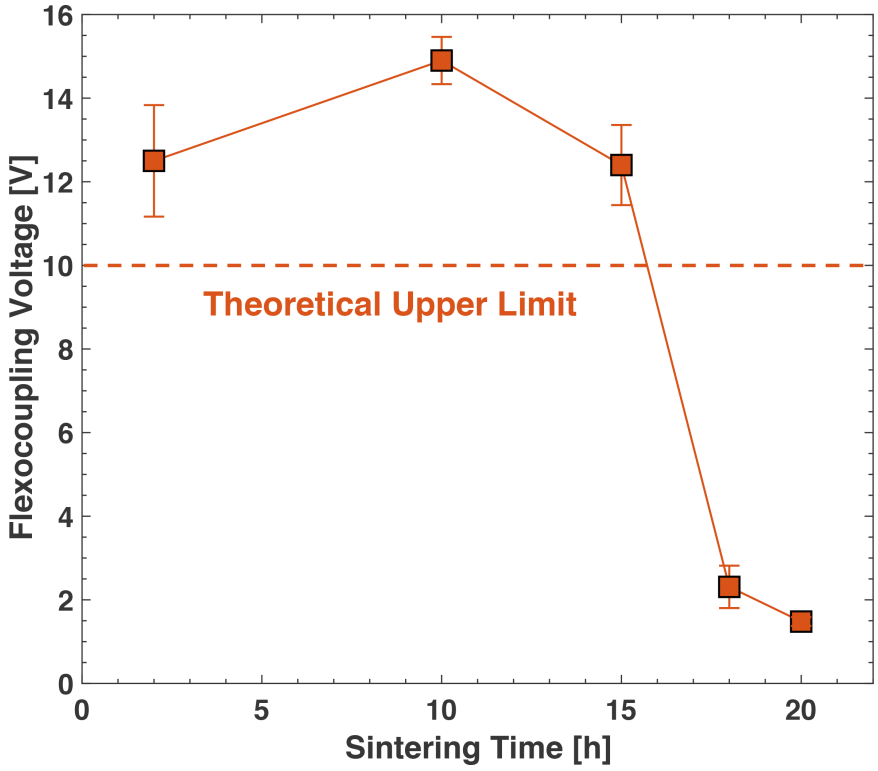

FIGURE 3.4.3. Experimental results of FcVs of various STO samples. Despite differences in the dielectric constant between samples, the trend from Figure 3.4.2 remained largely consistent. In addition, the flexocoupling voltage of the samples sintered for short times (2, 10, and 15 hours) displayed flexocoupling voltages greater than the theoretical upper limit of 10V for simple ionic solids.[3, 11]

Several factors could have led to the results seen in the second series of FxE measurements, and a few are discussed below along with results from preliminary experiments that were designed to test these possible factors.

3.4.1 Impact of Different Instruments

The first factor to test is the impact of using different instruments. The second series of measurements were all performed on a new DMA and a new LIA. The choice of switching instruments was a consequence of occasional reliability issues with the original instruments. It must also be noted that the initial measurements were completed when the original instruments were functioning normally.

The simplest way to test instrument effects is to measure a sample with a known FxE coefficient on both the new and the old instruments and compare the two results. A single-crystal MgO sample (the same one used for benchmarking the dielectric constant measurements) was thus selected

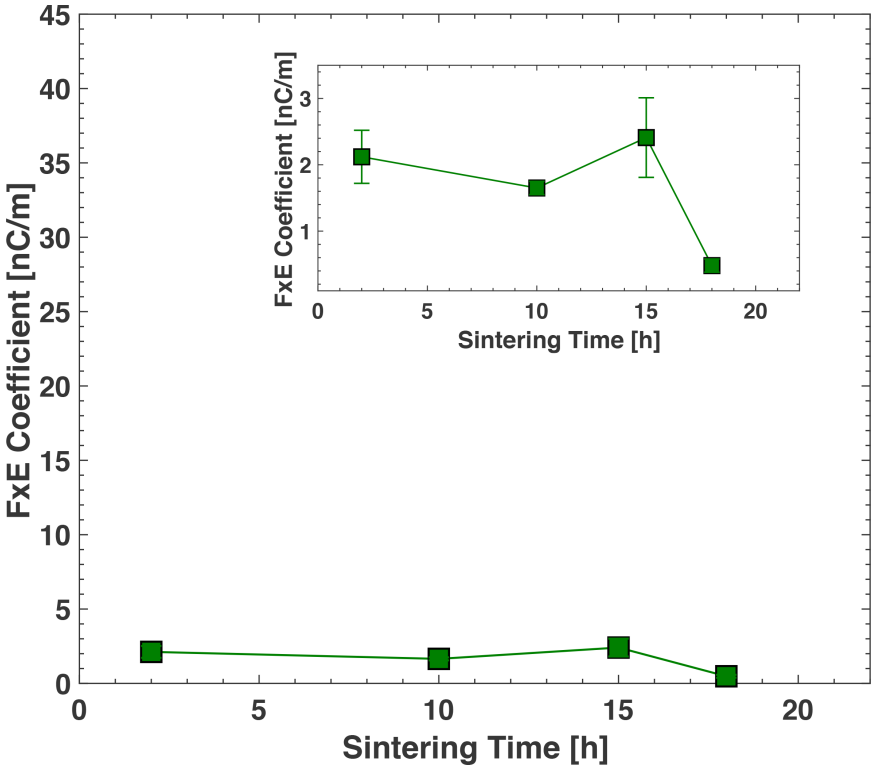

FIGURE 3.4.4. Experimental results of FxE coefficients of various STO samples measured for a second time. The samples are the same ones shown in Figure 3.4.2. The inset offers a close-up view of the spread in FxE coefficients. All of the samples shown have FxE coefficients significantly lower than before.

to be measured on the new instruments. The FxE coefficient of this sample had been previously characterized on the old instruments. Additionally, since the MgO sample is single-crystalline, the total FxE response of this sample should come entirely from the lattice response and remain relatively stable with all else held constant. The FxE measurements of the MgO sample are shown in Figure 3.4.5. The FxE coefficient measured using the new instruments is 3.04 ± 0.2 nC/m, which is very close to the value of 2.1 ± 0.3 nC/m measured using the old instruments.[38] The slight discrepancy is likely due to differences in instrument calibration. The result of this comparison suggests that switching instruments should not have been able to cause the more than an order of magnitude decrease observed between the initial and second series of FxE measurements.

3.4.2 Environmental Contamination

Once the reliability of the new instruments had been established, it was important to then test whether the observed decrease was caused by environmental contamination of the samples. The polycrystalline STO samples are inherently porous and it is very possible that various contami-

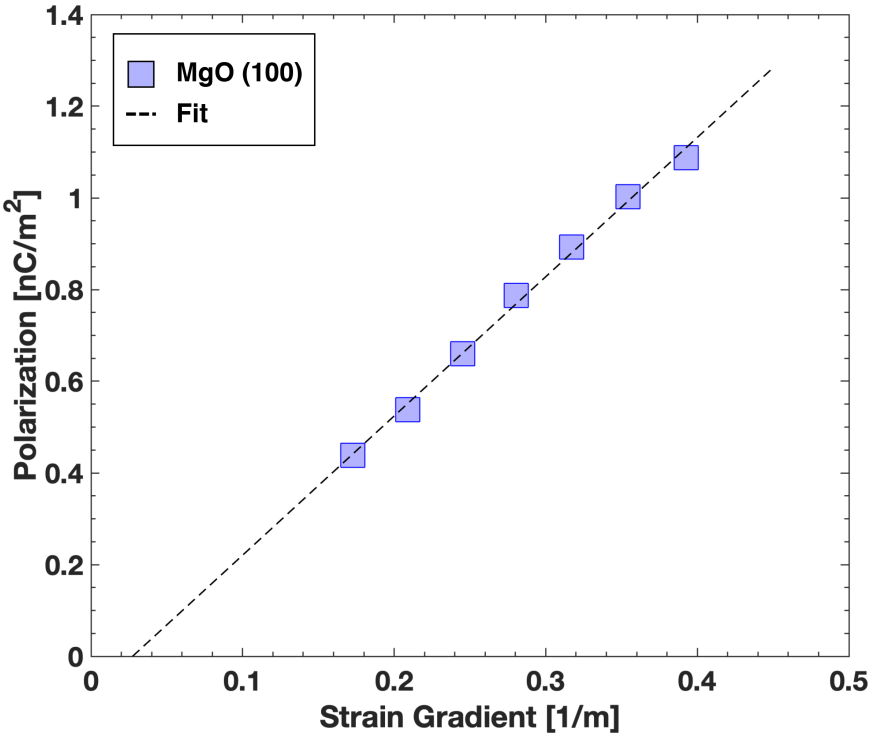

FIGURE 3.4.5. Experimental results of FxE coefficient measurement for an MgO (100) single crystal. Measurements were performed on the new DMA and the new LIA. The dashed lines represent a linear fit to the experimental data, with an R^2 value greater than 0.99. The slope of the fitted line is the FxE coefficient, which has a value of 3.04 ± 0.2 nC/m. The error is given by the 95% confidence interval of the linear fit.

nants, such as water and carbonaceous species, had adsorbed to exposed surfaces during handling and/or storage. It is possible that humidity level differences also had an impact, given the fact that the initial measurements were done in winter and the second series of measurements were done in spring. The aforementioned types of contamination could screen the FxE polarization on the sample surface, thus reducing the measured FxE response. All subsequent FxE measurements were done with new instruments.

The most direct way to test this hypothesis was to clean an STO sample by annealing (at a temperature lower than the sintering temperature to prevent grain growth) to remove adsorbates and then measure its FxE coefficient. The sample sintered for 15 hours was chosen for this experiment and was annealed at 600 °C for 6 hours in a box furnace to remove contaminants physiosorbed to the sample. During annealing, the sample was placed inside a clean glass container to prevent additional contamination inside the furnace. To minimize exposure to the atmosphere, after cooling down to room temperature, the sample was immediately measured. The results for the FxE coefficient measurements are shown in Figure 3.4.6. The FxE coefficient is determined to be 1.43 ± 0.1 nC/m, slightly lower than 2.41 ± 0.6 nC/m, which was determined in the second series of

measurements. The FxE coefficient of this cleaned sample still remained approximately a factor of 20 lower than it was in the original measurement, suggesting that environmental contamination did not have a large enough impact on the behavior of the FxE coefficient. Also, it is important to note that after annealing, the previously well-defined boundaries of the gold electrodes on the samples became less distinct, indicating that gold diffusion might have occurred. This means that experiments in which it is desirable to anneal a sample after gold deposition are ill-advised.

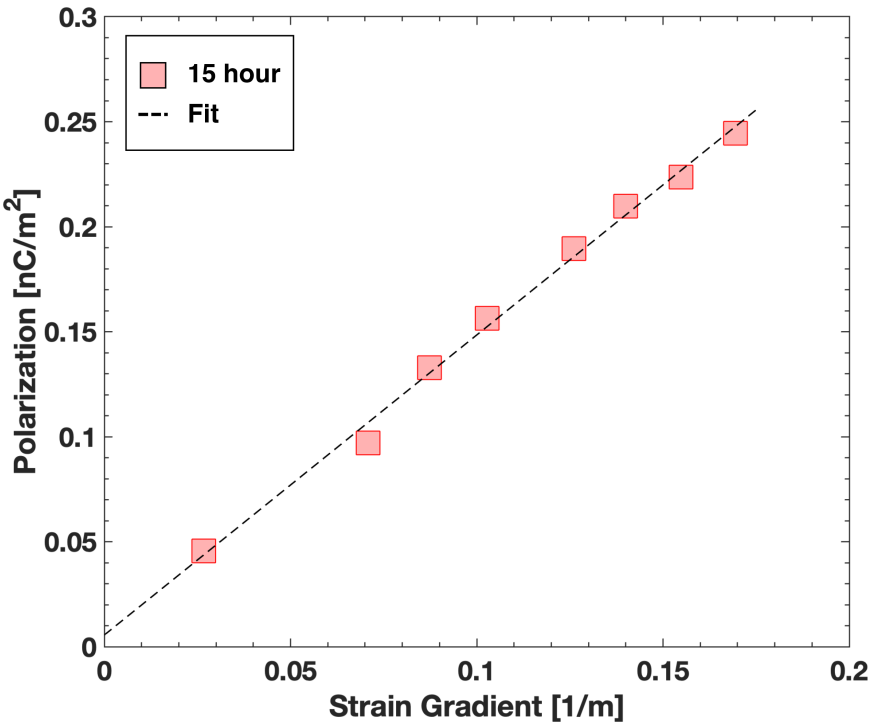

FIGURE 3.4.6. Experimental results of FxE coefficient measurement for the 15-hour STO sample after annealing for 6 hours at 600 °C. The dashed lines represent a linear fit to the experimental data, with an R^2 value greater than 0.99. The slope of the fitted line is the FxE coefficient, which has a value of 1.43 ± 0.1 nC/m. The error is given by the 95% confidence interval of the linear fit.

3.4.3 Time-Dependent FxE Degradation

Apart from environmental contamination, another general factor to consider was whether the sample itself had changed over time, either externally or internally. Considering that two months had passed between the two series of measurements, the STO samples might have experienced various forms of degradation. The quality of the electrodes could have deteriorated, leading to less polarization being measured for the same level of applied strain gradient; however, experiments with fresh electrodes show the same low FxE response. Alternatively, there might have been other features in the sample, such as residual strain gradients from the processing stage, which could

have relaxed over time. However, this implies that residual strain gradient contributions would also need to be included in explaining the initial measurements of large FxE coefficients in the STO samples. Finally, the nature of performing FxE coefficient measurements requires repeatedly bending brittle ceramic samples, which will likely induce internal cracking. It has been both theoretically and experimentally shown that polarizations near the tips of cracks in ferroelectric materials, such as $BaTiO_3$ (another well-studied oxide perovskite), are orders of magnitude greater than in the bulk material, as a consequence of the large strain gradients present near the crack tip.[39, 40] One or several of the features discussed above could be present in the STO samples, and would add complexity to the results interpretation.

Chapter 4

Conclusions and Suggestions for Future Work

This thesis represents an attempt to advance understanding of the role microstructure plays in flexoelectricity, with a specific focus on the impacts of grain size. Using polycrystalline STO ceramics prepared through a solid-state sintering process, it was demonstrated that by increasing the sintering time, and thus the average grain size, the magnitude of the FxE coefficients were decreased by a factor of 10, and approached the literature values for FxE coefficients of STO single crystals. This result lends evidence to the claim that the total FxE response of a polycrystalline sample can be separated into contributions from the intrinsic lattice and from the microstructure. In the context of STO, the primary microstructural contribution is considered to be from polar grain boundaries. As the average grain size was increased, the total grain boundary volume was decreased, and less polar grain boundaries were present in the samples. This likely resulted in the measured decrease in the FxE response of samples with larger grain sizes. Furthermore, unexpected decreases in the FxE coefficients were found upon re-measurement. Two months after the first measurements, the FxE coefficients of all samples had decreased by more than an order of magnitude. Preliminary experiments have been carried out to explore the possible effects of instrument error, environmental contamination, and other time-dependent degradation processes, such as strain relaxation and crack formation. In summary, the results of this work draw attention to the significance of microstructural effects on flexoelectricity in polycrystalline materials, and suggest a potential route to enhance flexoelectricity in STO by tuning the average grain size.

Much work, however, remains to be done to fully investigate the cause of unexpected decreases in the FxE coefficients over time. For example, the relative densities and porosities of the STO samples with different sintering times could be measured, both before and after undergoing FxE characterization, as a first step towards determining whether cracks could be responsible. Additionally, XRD experiments could be performed to investigate the presence of residual strain gradients. Finally, it might be instructive to employ techniques such as electron backscatter diffraction and transmission electron microscopy to explore whether FxE measurements can cause changes in grain and grain boundary orientations. Ultimately, these future directions of study will help to unravel the complex structure-property relations underlying flexoelectricity.

References

[1] T. Takenaka, H. Nagata, *Journal of the European Ceramic Society*, Elecroceramics IX **2005**, *25*, 2693–2700 (cit. on p. 1).

[2] S. M. Kogan, *Soviet Physics Solid State* **1964**, *5*, 2069–2070 (cit. on p. 1).

[3] P. Zubko, G. Catalan, A. K. Tagantsev, *Annual Review of Materials Research* **2013**, *43*, 387–421 (cit. on pp. 1, 2, 3, 13, 20, 26, 27).

[4] W. Ma, L. E. Cross, *Applied Physics Letters* **2001**, *78*, 2920–2921 (cit. on p. 1).

[5] W. Ma, L. E. Cross, *Applied Physics Letters* **2001**, *79*, 4420–4422 (cit. on p. 1).

[6] W. Ma, L. E. Cross, *Applied Physics Letters* **2002**, *81*, 3440–3442 (cit. on p. 1).

[7] W. Ma, L. E. Cross, *Applied Physics Letters* **2003**, *82*, 3293–3295 (cit. on p. 1).

[8] W. Ma, L. E. Cross, *Applied Physics Letters* **2005**, *86*, 072905 (cit. on p. 1).

[9] W. Ma, L. E. Cross, *Applied Physics Letters* **2006**, *88*, 232902 (cit. on p. 1).

[10] R. Newnham, *Properties of Materials: Anisotropy, Symmetry, Structure*, Oxford University Press, Oxford, New York, **2005**, 390 pp. (cit. on p. 2).

[11] P. V. Yudin, A. K. Tagantsev, *Nanotechnology* **2013**, *24*, 432001 (cit. on pp. 2, 3, 26, 27).

[12] A. P. Sutton, R. W. Balluffi, *Interfaces in crystalline materials*, Oxford University Press, New York, **2006** (cit. on p. 3).

[13] Y. A. Abramov, V. G. Tsirelson, V. E. Zavodnik, S. A. Ivanov, Brown I. D., *Acta Crystallographica Section B Structural Science* **1995**, *51*, 942–951 (cit. on p. 3).

[14] P. Zubko, G. Catalan, A. Buckley, P. R. L. Welche, J. F. Scott, *Physical Review Letters* **2007**, *99* (cit. on pp. 3, 13, 23, 25).

[15] N. D. Browning, J. P. Buban, H. O. Moltaji, S. J. Pennycook, G. Duscher, K. D. Johnson, R. P. Rodrigues, V. P. Dravid, *Applied Physics Letters* **1999**, *74*, 2638–2640 (cit. on p. 4).

[16] M. Kim, G. Duscher, N. D. Browning, K. Sohlberg, S. T. Pantelides, S. J. Pennycook, *Physical Review Letters* **2001**, *86*, 4056–4059 (cit. on p. 4).

[17] J. Petzelt, T. Ostapchuk, I. Gregora, I. Rychetský, S. Hoffmann-Eifert, A. V. Pronin, Y. Yuzyuk, B. P. Gorshunov, S. Kamba, V. Bovtun, J. Pokorný, M. Savinov, V. Porokhonskyy, D. Rafaja, P. Vaněk, A. Almeida, M. R. Chaves, A. A. Volkov, M. Dressel, R. Waser, *Physical Review B* **2001**, *64* (cit. on p. 4).

[18] P. Gao, S. Yang, R. Ishikawa, N. Li, B. Feng, A. Kumamoto, N. Shibata, P. Yu, Y. Ikuhara, *Physical Review Letters* **2018**, *120* (cit. on p. 4).

[19] J. Narvaez, F. Vasquez-Sancho, G. Catalan, *Nature* **2016**, *538*, 219–221 (cit. on p. 4).

[20] R. Glaister, *Proceedings of the IEE - Part B: Electronic and Communication Engineering* **1962**, *109*, 423–431 (cit. on p. 4).

[21] H. Neumann, G. Arlt, *Ferroelectrics* **1986**, *69*, 179–186 (cit. on p. 5).

[22] D. W. Richerson, W. E. Lee, *Modern Ceramic Engineering: Properties, Processing, and Use in Design, Fourth Edition*, CRC Press, Boca Raton, FL, **2018** (cit. on pp. 7, 8).

[23] B. D. Cullity, S. R. Stock, *Elements of X-ray Diffraction, Third Edition*, Prentice-Hall, New York, **2001** (cit. on pp. 9, 10).

[24] J. R. Macdonald, *Annals of Biomedical Engineering* **1992**, *20*, 289–305 (cit. on p. 10).

[25] J. Goldstein, D. E. Newbury, D. C. Joy, C. E. Lyman, P. Echlin, E. Lifshin, L. Sawyer, J. R. Michael, *Scanning Electron Microscopy and X-Ray Microanalysis*, 3rd ed., Springer US, **2003** (cit. on p. 11).

[26] E04 Committee, Test Methods for Determining Average Grain Size, ASTM International (cit. on p. 12).

[27] J. Schindelin, I. Arganda-Carreras, E. Frise, V. Kaynig, M. Longair, T. Pietzsch, S. Preibisch, C. Rueden, S. Saalfeld, B. Schmid, J.-Y. Tinevez, D. J. White, V. Hartenstein, K. Eliceiri, P. Tomancak, A. Cardona, *Nature Methods* **2012**, *9*, 676–682 (cit. on p. 12).

[28] M. I. Mendelson, *Journal of the American Ceramic Society* **1969**, *52*, 443–446 (cit. on p. 12).

[29] C. A. Mizzi, Flexoelectricity in Oxides, Qualifying Examination, Northwestern University (cit. on pp. 12, 13).

[30] N. A. Pertsev, A. K. Tagantsev, N. Setter, *Physical Review B* **2000**, *61*, R825–R829 (cit. on p. 13).

[31] K. P. Menard, *Dynamic Mechanical Analysis: A Practical Introduction*, CRC Press, New York, **2008** (cit. on p. 14).

[32] W. Schranz, *Phase Transitions* **1997**, *64*, 103–114 (cit. on p. 14).

[33] O. A. Bauchau, J. I. Craig in *Structural Analysis*, (Eds.: O. A. Bauchau, J. I. Craig), Solid Mechanics and Its Applications, Springer Netherlands, Dordrecht, **2009**, pp. 173–221 (cit. on p. 14).

[34] D. P. Blair, P. H. Sydenham, *Journal of Physics E: Scientific Instruments* **1975**, *8*, 621–627 (cit. on p. 15).

[35] R. J. Nelmes, G. M. Meyer, J. Hutton, *Ferroelectrics* **1978**, *21*, 461–462 (cit. on pp. 17, 18).

[36] M. Wintersgill, J. Fontanella, C. Andeen, D. Schuele, *Journal of Applied Physics* **1979**, *50*, 8259–8261 (cit. on pp. 21, 22).

[37] R. C. Neville, B. Hoeneisen, C. A. Mead, *Journal of Applied Physics* **1972**, *43*, 2124–2131 (cit. on p. 22).

[38] P. Koirala, C. A. Mizzi, L. D. Marks, *Nano Letters* **2018**, *18*, 3850–3856 (cit. on pp. 23, 25, 28).

[39] A. Abdollahi, C. Peco, D. MillÃ¡n, M. Arroyo, G. Catalan, I. Arias, *Physical Review B* **2015**, *92*, 094101 (cit. on p. 31).

[40] K. Cordero-Edwards, H. Kianirad, C. Canalias, J. Sort, G. Catalan, *Physical Review Letters* **2019**, *122*, 135502 (cit. on p. 31).